

# Antipolar ordering of topological charges and universality in active liquid crystals

Anand U. Oza<sup>1</sup> and Jörn Dunkel<sup>2</sup>

<sup>1</sup>*Courant Institute of Mathematical Sciences, 251 Mercer Street, New York, NY 10012, USA*

<sup>2</sup>*Department of Mathematics, Massachusetts Institute of Technology,  
77 Massachusetts Avenue, Cambridge, MA 02139-4307, USA*

(Dated: December 7, 2024)

Recent experiments demonstrated that ATP-driven microtubule-kinesin bundles can self-assemble into two-dimensional active liquid crystals that exhibit a rich creation and annihilation dynamics of topological defects, reminiscent of particle-pair production processes in quantum systems. This remarkable discovery has sparked considerable theoretical and experimental interest. Here, we present and validate a minimal continuum theory for this new class of active matter systems by merging universality ideas with the classical Landau-de Gennes theory. The resulting model agrees quantitatively with recently published data and, in particular, predicts a previously unexplained regime of antipolar order. Our analysis implies that active liquid crystals are governed by the same generic ordering principles that determine the non-equilibrium dynamics of dense bacterial suspensions and elastic bilayer materials. Moreover, the theory manifests a profound energetic analogy with strongly interacting quantum gases. Generally, our results suggest that complex nonequilibrium pattern-formation phenomena might be predictable from a few fundamental symmetry-breaking and scale-selection principles.

Active materials [1] assembled from intracellular components, such as DNA [2], microtubules and motor proteins [3–5] promise innovative biotechnological applications, from microscale transport and medical devices [2] to artificial tissues [1] and programmable soft materials [6–8]. Beyond their practical value, these systems challenge theorists to generalize equilibrium statistical mechanics to far-from-equilibrium regimes [9–19]. Recent experimental advances in the self-assembly and manipulation of colloids with DNA-mediated interactions [20–22] have stimulated theoretical analysis that may eventually help clarify the physical principles underlying self-replication [23–25] and evolution in viruses [26–28] and other basic biological systems. Yet, despite some partial progress [10, 16, 17, 29–32], our conceptual understanding of active materials, and living matter in general, remains far from complete. We do not know whether, or under which conditions, ‘universality’ ideas [33] that have proved powerful in the description of equilibrium systems can be generalized to describe collective dynamics of active matter. This deficit may be ascribed to the fact that mathematical models have been successfully tested against experiments in only a few instances [3, 4, 34–37].

The hypothesis of universal pattern formation mechanisms in soft and active matter systems received preliminary support from recent experiments on elastic bilayer systems [38] and dense bacterial suspensions [34, 35, 39]. Specifically, it was found that, despite their distinct microscopic compositions, these two classes of systems can be described quantitatively in terms of generic fourth-order partial differential equations (PDEs) for scalar and vector fields [34, 35, 38]. The striking mathematical similarities of the two field theories suggest that complex nonequilibrium pattern-formation phenomena [40] might be predictable from a few fundamental symmetry-breaking and scale-selection principles, analogous to the phase transitions in equilibrium thermodynamics [41].

To recall how universality concepts are connected to higher-order PDEs, we may consider a macroscopic order-parameter field  $\phi(t, \mathbf{r})$ , which could represent concentration, average gene expression profiles, color or any other relevant tensor field describing a collection of individual components in a physical or biological system. In general, the dynamics of  $\phi(t, \mathbf{r})$  and its associated Fourier modes  $\hat{\phi}(t, \mathbf{k})$  will be highly nonlinear. The universality hypothesis postulates that microscopically distinct systems exhibit similar macroscopic behavior when they share the mathematical structure of the leading-order terms in their field equations, which are thought to arise from Taylor series-type expansions. For example, if a scalar order-parameter field  $\phi$  is symmetrically distributed around zero, and  $\phi$  prefers to take one of two characteristic states  $\pm\phi_c$ , then one can expect a leading-order dynamics described by

$$\partial_t \phi = a\phi + b\phi^3 + \dots \quad (1)$$

where  $\sqrt{-a/b} = \phi_c$  and  $a > 0, b < 0$  to ensure stability of the fixed points  $\pm\phi_c$ . Similarly, when patterns of length scale  $\Lambda$  and hence wavenumbers  $k_\Lambda = 2\pi/\Lambda$  are selected in an otherwise isotropic spatial setting, the leading order dynamics in Fourier-space may be described by

$$\partial_t \hat{\phi} = (\alpha|\mathbf{k}|^2 + \beta|\mathbf{k}|^4 + \dots)\hat{\phi} \quad (2)$$

where  $\sqrt{-\alpha/(2\beta)} = k_\Lambda$  with  $\alpha > 0, \beta < 0$  to prevent blow-up at small wavelengths. Identifying  $\nabla \leftrightarrow -i\mathbf{k}$ , we may combine Eqs. (1) and (2) to obtain a fourth-order PDE in position space [40]:

$$\partial_t \phi = a\phi + b\phi^3 - \alpha\nabla^2 \phi + \beta(\nabla^2)^2 \phi. \quad (3)$$

Thus, intuitively, Eq. (1) identifies the most commonly observed field values with fixed points, while Eq. (2) formalizes the fact that the most commonly observed patterns outcompete other scales, because their associated

Fourier modes grow most rapidly. The universality hypothesis assumes that expansions of the above type govern the dynamics of a wide range of many-particle systems, with microscopic properties entering through the coefficients ( $a, b, \dots, \alpha, \beta, \dots$ ). Despite their success in describing conventional physical systems [33, 40, 41], the general applicability of these ideas to active matter systems has yet to be examined through detailed comparison between theory and experiment.

Recently discovered 2D active liquid crystal (ALC) analogs [5, 42–45] comprise an important class of non-equilibrium systems that allows further tests of universality concepts [33] and specific theories. ALCs are assemblies of rod-like particles that exhibit non-thermal collective excitations due to steady external [42, 43] or internal [5, 45] energy input. At high concentrations, ALCs form an active nematic phase characterized by dynamic creation and annihilation of topological defects [5, 42, 45], reminiscent of spontaneous particle-pair production in quantum systems. This phenomenon was demonstrated recently [5, 45, 46] for ATP-driven microtubule-kinesin bundles trapped in flat and curved interfaces. Moreover, these experiments [46] revealed an unexpected nematic ordering of topological defects which is unaccounted for in current theoretical models. Understanding the emergence of such topological super-structures is crucial for the development and control of new materials, as recently demonstrated for colloidal liquid crystals [47–49].

We here develop and validate a closed continuum theory for dense ALCs by generalizing the higher-order scalar and vector theories of soft elastic materials [38] and bacterial fluids [34, 35] to matrix-valued fields. Conceptually, our approach unifies the classic Landau-de Gennes description of passive LCs [41] with the Swift-Hohenberg theory [50] of pattern formation. A systematic comparison with recently published data confirms agreement between our theory and experiments [5, 46]. In addition, we present an equivalent complex scalar field representation [14, 51] that reveals an otherwise hidden analogy with a generalized Gross-Pitaevskii theory [52, 53] of strongly coupled many-body quantum systems [54–57]. In the case of normal dispersion (corresponding to  $\alpha < 0$  in Eq. (2)), the celebrated LC-superconductor correspondence [51, 58] has helped elucidate profound parallels between the smectic phase in passive LCs and the Abrikosov vortex lattices in type-II superconductors [59, 60]. The results below indicate that a similar analogy may exist between ALCs and Bose-Einstein/Fermi condensates with anomalous dispersion [55–57] (corresponding to  $\alpha > 0$  in Eq. (2)), suggesting that ALCs can offer insights into the dynamics of these quantum systems and *vice versa*.

## RESULTS

**Experimental conditions.** To place a stringent test on the applicability of universality concepts [33] to active matter systems, the theory developed below aims

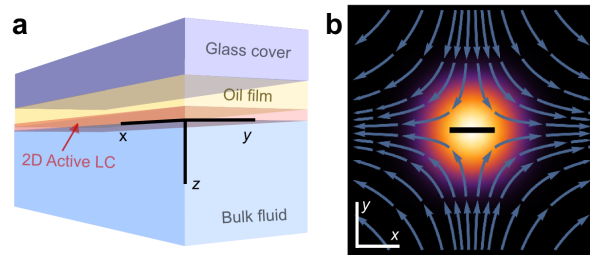


FIG. 1: (A) Schematic of the experimental setup reported in Ref. [5, 46], not drawn to scale. A thin oil film (thickness  $\sim 3 \mu\text{m}$ ) separates a 2D ALC layer ( $\sim 0.2 - 1.0 \mu\text{m}$ ) at the oil-water interface from a solid glass cover. Liquid can be exchanged between the ALC layer and bulk fluid, resulting in compressible 2D interfacial flow that is strongly damped by the nearby no-slip glass boundary and the viscous oil layer. (B) Extensile 2D dipole flow in the interface as predicted by the overdamped closure condition (7) for  $D > 0$  and  $Q = (\lambda, 0; 0, -\lambda)$  with  $\lambda = \exp(-r^2)$ . The central horizontal bar indicates the unit director axis, and background colors the nematic order parameter  $S \sim \lambda$ .

to rationalize simultaneously the results from two recent experimental studies [5, 46]. In these experiments, ATP-driven microtubule-kinesin bundles were found to self-assemble into a dense quasi-2D ALC layer at an oil-water interface parallel to a planar solid boundary (Fig. 1a). This ‘wet’ ALC was found to exhibit clear local nematic alignment of bundles, persistent annihilation and creation dynamics of topological defects [5], and remarkable nematic order of the defect orientations in thin layers [46]. Although a large number of unknown parameters has prevented detailed quantitative comparisons between theory and experiment, several recently proposed multi-order-parameter models of 2D ALC systems [14, 18, 61, 62] were able to reproduce qualitatively selected aspects of these observations. However, they generally fail to explain the observed topological defect order, primarily for two reasons. First, these models typically assume divergence-free 2D fluid flow within the ALC layer, which is a valid approximation for isolated free-standing film experiments [63] but does not account for fluid exchange between the 2D interface and bulk in the ALC experiments (Fig. 1a). As is known for classical turbulence [64, 65], small-scale energy input can trigger turbulent upward cascades in incompressible 2D flow. Thus, topological defect dynamics in the current standard models is dominated by artificially enhanced hydrodynamic mixing due to an unjustified 2D incompressibility assumption. Second, a relevant yet previously ignored effect is damping from the nearby boundaries, which may promote topological defect ordering. To overcome such limitations and establish a quantitative description of the experiments [5, 46], we next construct a closed continuum theory for the nematic order-parameter tensor-field  $Q(t, \mathbf{r})$  of dense ALCs, by combining universality ideas with a self-consistent hydrodynamic closure condition.

**Theory.** Traditional multi-field models [61, 62] aim to describe the 2D nematic phase of a dense ALC suspension by coupling the filament concentration  $c(t, \mathbf{r})$  and the nematic order tensor  $Q(t, \mathbf{r})$  to an incompressible 2D flow field  $\mathbf{v}(t, \mathbf{r})$  that satisfies  $\nabla \cdot \mathbf{v} = 0$  in the interface plane  $\mathbf{r} = (x, y)$ . The nematic order parameter  $S(t, \mathbf{r})$  is proportional to the larger eigenvalue of  $Q$ , and the filaments are oriented along the corresponding eigenvector, or director  $\mathbf{d}(t, \mathbf{r})$ . To construct an alternative closed-form theory for the symmetric traceless  $2 \times 2$ -tensor field  $Q$ , we start from the generic transport law

$$\partial_t Q + \nabla \cdot (\mathbf{v}Q) - \kappa[Q, \omega] = -\frac{\delta \mathcal{F}}{\delta Q} \quad (4)$$

where  $\omega = [\nabla \mathbf{v} - (\nabla \mathbf{v})^\top]/2$  is the vorticity tensor,  $[A, B] = AB - BA$  the commutator of two matrices and  $\mathcal{F}[Q] = \int d^2r F$  an effective free energy. Focussing on dense suspensions as realized in the experiments [5, 46], we neglect fluctuations in the microtubule concentration,  $\nabla c \equiv 0$ . It is important, however, that  $\nabla \cdot (\mathbf{v}Q) \neq \mathbf{v} \cdot \nabla Q$  when  $\nabla \cdot \mathbf{v} \neq 0$ , which is typically the case when fluid can enter and leave the interface. Combining Landau-de Gennes theory [41] with Swift-Hohenberg theory [50], we postulate the free-energy density (Supplementary Information)

$$F = \text{Tr} \left\{ -\frac{a}{2} Q^2 + \frac{b}{4} Q^4 - \frac{\gamma_2}{2} (\nabla Q)^2 + \frac{\gamma_4}{4} (\nabla \nabla Q)^2 \right\} \quad (5)$$

with  $a, b > 0$  for the nematic phase. Assuming  $\gamma_2$  can have either sign, ultraviolet stability requires  $\gamma_4 > 0$ . For  $\gamma_2 < 0$ ,  $F$  possesses a homogeneous nematic ground-state manifold, whereas for  $\gamma_2 > 0$  a pattern of characteristic wavelength  $\Lambda \sim \sqrt{\gamma_4/\gamma_2}$  becomes energetically favorable, as shown below. We note that extra terms coupling the nematic field to the induced flow may be added to Eq. (4), an example being  $S(\nabla \mathbf{v} + (\nabla \mathbf{v})^T)$  [62], but we neglect such effects in the interest of constructing a minimal mathematical theory capable of capturing key experimental observations.

To obtain a closed  $Q$ -model, we relate the 2D flow field  $\mathbf{v}$  to  $Q$  through the linearly damped Stokes equation [66]

$$-\eta \nabla^2 \mathbf{v} + \nu \mathbf{v} = -\zeta \nabla \cdot Q \quad (6)$$

where  $\eta$  is the viscosity and the rhs. represents active stresses [10, 61] with  $\zeta > 0$  for extensile ALCs (Fig. 1b). A pressure term does not appear in Eq. (6) because the interfacial flow is not assumed to be incompressible and concentration fluctuations are neglected. The  $\nu$ -term in the force balance (6) accounts for friction from the nearby no-slip boundary in the Hele-Shaw [66] approximation (Fig. 1a). In the overdamped regime  $\nu \Lambda^2/\eta \gg 1$ , we deduce from Eq. (6) the closure condition

$$\mathbf{v} = -D \nabla \cdot Q, \quad D = \zeta/\nu. \quad (7)$$

Equation (7) is conceptually similar to closure conditions proposed previously for active polar films

[67]. Importantly, Eq. (7) predicts divergent interfacial flow,  $\nabla \cdot \mathbf{v} \neq 0$ , and hence fluid transport perpendicular to the interface wherever  $\nabla \nabla : Q \neq 0$ . Inserting (7) into (4) yields a closed  $Q$ -theory in which periodic director patterns corresponding to local minima of the free energy  $\mathcal{F}$  can become mixed by self-generated interfacial flow.

**Complex representation & ALC-quantum analogy.** The traditional characterization of 2D nematic order in terms of the symmetric traceless  $2 \times 2$  matrix field  $Q = (\lambda, \mu; \mu, -\lambda)$  is redundant, for only two real scalar fields  $\lambda(t, \mathbf{r})$  and  $\mu(t, \mathbf{r})$  are needed to specify the nematic state at each position  $\mathbf{r} = (x, y)$ . To obtain an irreducible representation [14, 51] we define the complex position coordinate  $z = x + iy$ , velocity field  $v(t, z) = u + iw$  and complex order parameter  $\psi(t, z) = \lambda + i\mu$ , such that  $S = 2|\psi|$ . In terms of the Wirtinger gradient operator  $\partial = \frac{1}{2}(\partial_x - i\partial_y)$ , the 2D Laplacian takes the form  $\nabla^2 = 4\bar{\partial}\partial$  and the closure condition (7) reduces to  $v = -2D\partial\psi$ . Denoting the real and imaginary parts of an operator  $\mathcal{O}$  by  $\Re\{\mathcal{O}\}$  and  $\Im\{\mathcal{O}\}$ , Eqs. (4) and (5) may be equivalently expressed as

$$\partial_t \psi + \mathcal{A}_\psi \psi = -\frac{\delta \mathcal{G}}{\delta \bar{\psi}} \quad (8)$$

where the self-advection operator is given by

$$\mathcal{A}_\psi = -4D \Re\{(\partial^2 \psi) + (\partial \psi)\partial\} + 4\kappa D i \Im\{\partial^2 \psi\} \quad (9)$$

and the free energy  $\mathcal{G}[\psi, \bar{\psi}] = \int dz G$  has the density

$$G = -a|\psi|^2 + \frac{b}{2}|\psi|^4 + \gamma_2 \bar{\psi}(4\bar{\partial}\partial)\psi + \gamma_4 \bar{\psi}(4\bar{\partial}\partial)^2\psi. \quad (10)$$

For  $\gamma_2 < 0$  and  $\gamma_4 \rightarrow 0$ , Eq. (10) reduces to the energy density of the Gross-Pitaevskii mean-field model [52, 53] for weakly interacting boson gases. Historically, this limit case has been crucial [51, 58] for elucidating the analogy between the smectic phase of passive LCs and the Abrikosov flux lattice in type-II superconductors [59, 60]. For  $\gamma_2, \gamma_4 > 0$ , Eq. (10) effectively describes double-well dispersion [54], as recently realized for quasi-momenta in spin-orbit-coupled Bose-Einstein condensates [55, 57] and Fermi gases [56]. This fact establishes an interesting connection between dense ALCs and strongly coupled quantum systems: when self-advection is negligible ( $D \rightarrow 0$ ), the fixed point configurations of Eq. (8) coincide with the ‘eigenstates’ of generalized Gross-Pitaevskii models that incorporate wavelength selection.

**Stability analysis.** The qualitative model dynamics is not significantly altered for moderate values of  $\alpha$  (Movies S1 and S2), so we neglect the commutator term by setting  $\kappa = 0$  from now on (see Supplementary Information for  $\kappa > 0$ ). To understand the properties of Eqs. (8)–(9) when self-advection is relevant, we perform a fixed point analysis of the rescaled dimensionless equation (Supplementary Information)

$$\partial_t \psi - 4D \Re\{(\partial^2 \psi) + (\partial \psi)\partial\} \psi = \left(\frac{1}{4} - |\psi|^2\right) \psi - \gamma_2 (4\bar{\partial}\partial)\psi - (4\bar{\partial}\partial)^2 \psi, \quad (11)$$

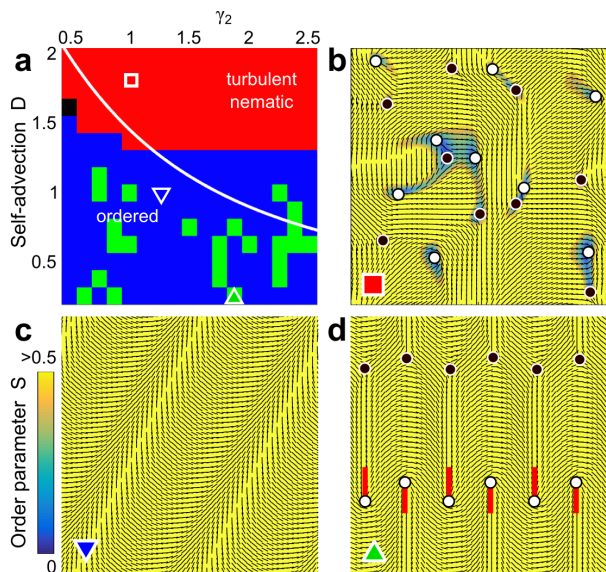


FIG. 2: Phase diagram obtained from simulations of Eq. (11) for one particular set of random initial conditions showing the emergence of turbulent nematic states for supercritical active self-advection. (a) We observe convergence to defect-free stripes (blue, panel c, Movie S3), time-periodic and stationary defect lattice solutions (green, panel d, Movie S4), periodic defect creation and annihilation events (black, Movie S6), and chaotic dynamics (red, panel b, Movie S1). The white line indicates the analytical estimate  $D_c = 2(-\gamma_2 + \sqrt{\gamma_2^2 + 2})$  for the transitions between ordered and chaotic states. (b-d) Examples of the states identified in a with  $-\frac{1}{2}$ -defects (black) and  $+\frac{1}{2}$ -defects (white). Panel d highlights the antipolar ordering of  $+\frac{1}{2}$ -defect orientations (red bars); see also Movie S5 for a realization of this state in a larger simulation domain.

by focussing on the uniform state  $\psi_* = \frac{1}{2}e^{i2\theta}$ , which corresponds to a nematic order parameter value  $S = 1$  and homogeneous director angle  $\theta$  relative to the  $x$ -axis. Considering wave-like perturbations  $\psi = \psi_* + \hat{\epsilon}(t)e^{i\mathbf{k}\cdot\mathbf{r}}$  with  $|\hat{\epsilon}| \ll 1$  and extensile ALCs with  $D > 0$ , one finds that  $\psi_*$  is unstable when  $\gamma_2 > 0$  (Supplementary Information). For subcritical self-advection,  $D < D_c = 2(-\gamma_2 + \sqrt{\gamma_2^2 + 2})$ , the most unstable mode  $\mathbf{k}_* = k_*(\cos \phi_*, \sin \phi_*)$  is aligned parallel to the director,  $(k_*, \phi_*) = (\sqrt{\gamma_2}/(2\gamma_4), \theta)$ , suggesting the formation of stripe patterns with typical wavelength  $\Lambda \approx \sqrt{8\pi^2\gamma_4/\gamma_2}$ . By contrast, for supercritical advection,  $D > D_c$ , the most unstable mode propagates perpendicular to the director,  $(k_*, \phi_*) = (\sqrt{(2\gamma_2 + D)/(4\gamma_4)}, \theta + (\pi/2))$ , suggesting the possibility of transverse mixing.

**Phase diagram.** To investigate the nonlinear dynamics of Eq. (11), we implemented a Fourier pseudospectral algorithm with modified Runge-Kutta time-stepping [68] (Methods) and so evolved the real and imaginary parts of  $\psi(t, z)$  in time for periodic boundary conditions in space. A numerically obtained  $(\gamma_2, D)$ -phase diagram for random initial conditions confirms the existence of

a turbulent nematic phase if active self-advection is sufficiently strong (Fig. 2a,b; Movie S1). Ordered configurations prevail at low activity (Fig. 2a,c,d; Movies S3, S4 and S6). Although the ground-states of the free energy (5) are in general not homogeneous, the critical curve separating the two regimes is in fair agreement with the estimate  $D_c = 2(-\gamma_2 + \sqrt{\gamma_2^2 + 2})$  from linear stability of the homogenous state (white line in Fig. 2a). For subcritical values of the advection parameter  $D$ , we observe either defect-free ground-states or long-lived lattice-like states exhibiting ordered defect configurations (Fig. 2c,d). Numerical free-energy calculations show that defect-free states (Fig. 2c) typically have slightly lower energies than the lattice states (Fig. 2d). Regarding the subsequent comparison of theory and experiment, it is important to note that the lattices are also found in simulations with a large domain (Movie S5), and generally exhibit antipolar ordering of  $+\frac{1}{2}$ -defects (Fig. 2d).

**Theory vs. experiment.** To test our theory systematically against existing experimental data [5, 46], we analyze defect-pair dynamics, global defect ordering and defect statistics in the turbulent nematic phase.

Spontaneous defect-pair creation and subsequent propagation, as reported in recent ALC experiments [5] and observed in our simulations, are compared in Fig. 3. In the experimental system [5], a  $(+\frac{1}{2}, -\frac{1}{2})$ -defect pair is created when fracture along incipient crack regions [18] becomes energetically more favorable than buckling. After creation, the  $+\frac{1}{2}$ -defect moves away rapidly whereas the position of the  $-\frac{1}{2}$ -defect remains approximately fixed for up to several seconds (Fig. 3a). Our simulations of the minimal model defined in Eq. (11) accurately reproduce the details of the experimentally observed dynamics (Fig. 3b; Movies S1 and S2).

Another striking and unexplained experimental observation [46] is the emergence of orientational order of  $+\frac{1}{2}$ -defects in thin ALC layers (Fig. 4). Using the setup illustrated in Fig. 1a, recent experiments [46] demonstrated nematic alignment of  $+\frac{1}{2}$ -defects in thin ALC layers of thickness  $h \sim 250$  nm (Fig. 4a), whereas thicker ALC layers with  $h \sim 1 \mu\text{m}$  showed no substantial orientational order on large scales (Fig. 4b). To investigate whether our theory can account for these phenomena, we tracked defect positions  $\mathbf{r}_i$  (Methods) and defect orientations  $\mathbf{n}_i = \nabla \cdot \mathbf{Q}(\mathbf{r}_i)/|\nabla \cdot \mathbf{Q}(\mathbf{r}_i)|$  [69] in simulations for different values of the advection parameter  $D = \zeta/\nu$ , since Brinkmann-type scaling arguments suggest that  $D$  increases with the ALC layer thickness,  $D \propto 1/\nu \propto h^p$  with  $p \in [1, 2]$ . For weakly supercritical advection,  $D \gtrsim D_c$ , we find that Eq. (11) predicts robust antipolar alignment of  $+\frac{1}{2}$ -defects (Fig. 4c). In our simulations, this ordering decreases as the effective mixing strength  $D$  increases (Fig. 4d), consistent with the experimental results [46] for thicker ALC layers (Fig. 4b). Similar ordering was observed in simulations that incorporated alignment of the nematic field near the horizontal boundaries of the simulation box (Supplementary Information; Fig. S5). To quantify the de-

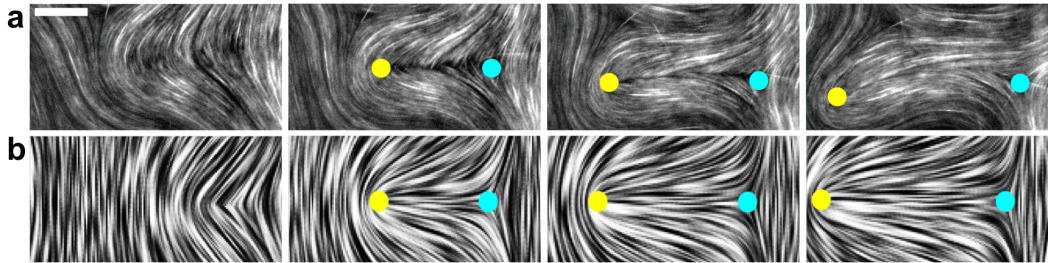


FIG. 3: Defect-pair creation and propagation in experiment and theory. (a) Experimentally observed dynamics of a defect pair, spontaneously produced by buckling and subsequent fracture of filaments; adapted with permission from Fig. 3d in Ref. [5]. Scale bar  $20 \mu\text{m}$ , time lapse 15 s. (b) Line integral convolution (LIC) plot of the director fields showing the spontaneous creation and propagation of a defect-pair in a simulation of Eq. (11) for  $D = 1.5$ ,  $\gamma_2 = 1$ . As in the experiments,  $+\frac{1}{2}$ -defects (yellow) generally move faster than  $-\frac{1}{2}$ -defects (light blue), cf. Fig. 6.

gree of orientational order, we recorded the distances  $d_{ij}$  between all  $+\frac{1}{2}$ -defect pairs  $(i, j)$  as well as their relative orientation angles  $\theta_{ij} = \cos^{-1}(\mathbf{n}_i \cdot \mathbf{n}_j) \in [0, \pi]$ . The resulting pair-orientation distributions  $p(\theta|r)$ , and polar and nematic correlation functions,  $P(r) = \langle \mathbf{n}_i \cdot \mathbf{n}_j \rangle_r$  and  $S(r) = 2\langle (\mathbf{n}_i \cdot \mathbf{n}_j)^2 \rangle_r - 1$ , are shown in Fig. 5, with  $\langle \cdot \rangle_r$  denoting an average over pairs of defects separated by a dis-

tance  $r$ . The local maxima in the orientation distribution at  $\theta = 0$  and  $\theta = \pi$  signal antipolar ordering (Fig. 5a), which is also reflected in the oscillatory behavior of the polar and nematic correlation functions (Fig. 5c,d). The diminished intensity of the local maxima for larger values of  $D$  indicates that enhanced hydrodynamic mixing reduces orientational order (Fig. 5c,d).

Lastly, we test the theoretically predicted defect statistics against a separate experimental data set kindly pro-

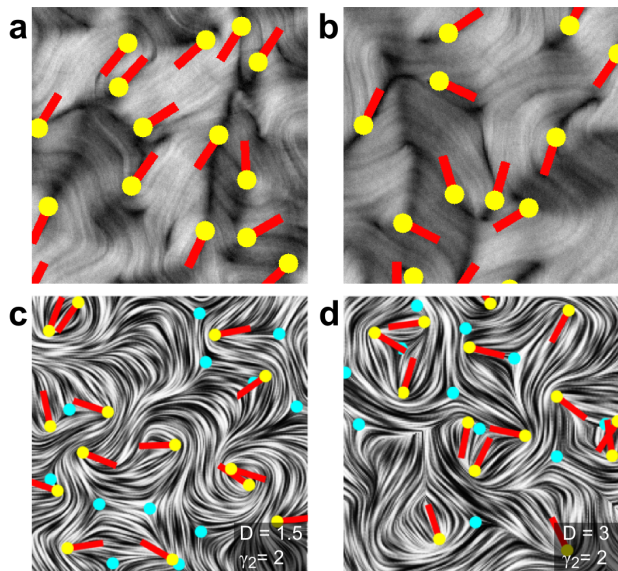


FIG. 4: Strong and weak antipolar ordering of  $+\frac{1}{2}$ -defects as (a,b) observed in experiments [46] and (c,d) predicted by our theory based on 2D simulations with periodic boundary conditions. Light-blue markers:  $-\frac{1}{2}$ -defects. Yellow markers:  $+\frac{1}{2}$ -defects. Red bars: orientation of  $+\frac{1}{2}$ -defects. (a)  $+\frac{1}{2}$ -defects in thin ALC films (thickness  $h \sim 250 \text{ nm}$ ) show strong nematic alignment. (b)  $+\frac{1}{2}$ -defects in thicker ALC films ( $h \sim 1 \mu\text{m}$ ) are more disordered. (c,d) For weak effective hydrodynamic coupling  $D$ , simulations show antipolar ordering, which is inhibited for larger values of  $D$ . The average number of defects in the full simulation box is approximately (c) 240 and (d) 350. Figures a and b kindly provided by S. DeCamp and Z. Dogic.

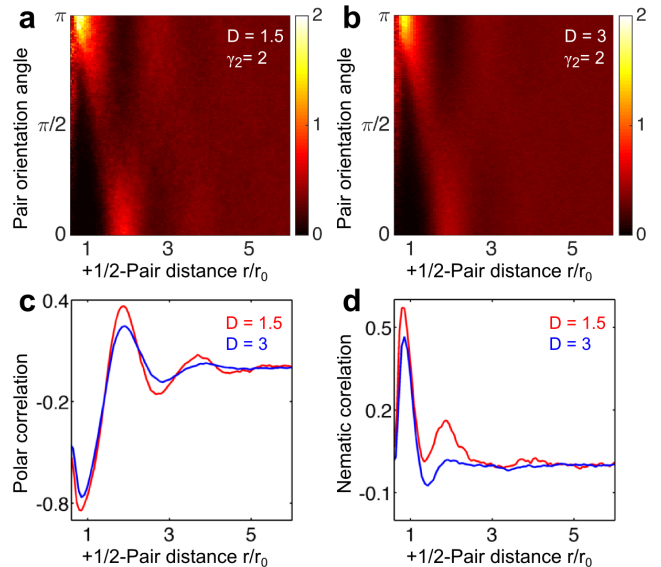


FIG. 5: Increasing activity and film thickness decrease antipolar ordering in simulations. (a,b) Maxima of the numerically obtained local pair orientation PDFs  $p(\theta_{ij}|r)$  signal antipolar local ordering of  $+\frac{1}{2}$ -defects as they are separated by the typical defect-lattice spacing. The defect distance  $r$  is specified in units of the mean nearest-neighbor distance  $r_0$  between  $+\frac{1}{2}$ -defects. (c,d) Polar  $P(r)$  and nematic  $S(r)$  correlation functions for  $D = 1.5$  (red) and  $D = 3$  (blue). Increasing the effective hydrodynamic coupling  $D$  leads to stronger mixing and hence decreases nematic order. The simulation parameters correspond to those given in Fig. 4c,d.

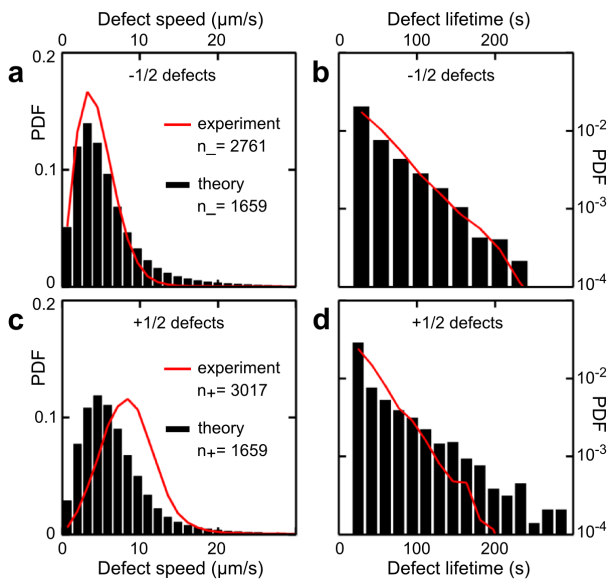


FIG. 6: Quantitative comparison of defect statistics between predictions of Eq. (11) and experimental data [46], using the parameter estimation procedure described in the text. For  $-\frac{1}{2}$ -defects, both (a) speed distribution and (b) lifetime distribution agree well. (c) For  $+\frac{1}{2}$ -defects, experimentally measured speed values are slightly larger, as our model assumes a strongly overdamped limit. (d) Simulations with periodic boundary conditions (Movie S7) predict a low-probability tail of large lifetimes which is not visible in the experiment, likely due to its restricted field of view or additional noise. Dimensionless simulation parameters  $D = 1.75$  and  $\gamma_2 = 1$  translate into the following dimensional values:  $a = 0.08 \text{ s}^{-1}$ ,  $b = 0.32 \text{ s}^{-1}$ ,  $D = 1791 \mu\text{m}^2/\text{s}$ ,  $\gamma_2 = 1024 \mu\text{m}^2/\text{s}$ ,  $\gamma_4 = 3.28 \times 10^6 \mu\text{m}^4/\text{s}$ . The numbers  $n_{\pm}$  reflect the number of  $\pm\frac{1}{2}$ -defects tracked, and the simulation domain contained  $\sim 130$  defects at any given time.

vided by DeCamp *et al.* (private communication). Since our simulations are performed in dimensionless units, there is freedom to choose a characteristic lengthscale  $l_0$  and timescale  $t_0$ . To relate theory and experiments, we determine  $(l_0, t_0)$  such that the joint mean speed and mean lifetime of  $\pm\frac{1}{2}$ -defects match the experimental values  $\bar{v} = 6.6 \mu\text{m}/\text{s}$  and  $\bar{\tau} = 52.8 \text{ s}$ . After fixing these global scales, we can compare details of the speed and lifetime distributions (Fig. 6). To this end, we first locate the ‘best-fit’ simulation parameters in the  $(\gamma_2, D)$ -parameter space explored in the phase diagram (Fig. 2a). This procedure identifies  $\gamma_2 = 1, D = 1.75$  as the best-match parameters, although nearby parameter values and simulations with  $\kappa = 1$  produce fits of similar quality, corroborating the robustness of the model (Fig. S4). For  $-\frac{1}{2}$ -defects, we find adequate agreement between experiment and theory for speed and lifetime probability density functions (PDFs), as evident from Fig. 6a,b. For  $+\frac{1}{2}$ -defects, simulation results also agree well with the experimental measurements (Fig. 6c,d), but one notices two systematic differences. First, while the peak heights

of the PDFs agree within a few percent, experimentally measured speed values for  $+\frac{1}{2}$ -defects are on average slightly larger than theoretically predicted values (Fig. 6c). Second, simulation data predict a miniscule tail-fraction of long-living  $+\frac{1}{2}$ -defects not detected in the experiment (Fig. 6d). In addition, based on the experimental density estimate of  $30 \text{ defects}/\text{mm}^2$  [46], we find that the defect density at any given time in the ‘best-fit’ simulation is  $\sim 2.3\times$  lower than in the experiments. As discussed below, such deviations can be explained plausibly by specific model assumptions. Taken together, the above results confirm that the minimal model defined by Eq. (11) provides a satisfactory qualitative and quantitative description of the main experimental results [5, 46].

## DISCUSSION

**Universality.** Equations (5) and (10) epitomize the idea of ‘universality’ in spatio-temporal pattern formation [50, 70], as outlined in the introduction. The free-energy expressions contain the leading-order terms of generic series expansions in both order-parameter space and Fourier space, consistent with spatial and nematic symmetries. When considering passive systems with a preference for homogenization ( $\gamma_2 < 0$ ), it usually suffices to keep only the quadratic gradient terms. By contrast, for pattern forming systems, the coefficient in front of the lowest-order gradient contribution can change sign [38, 50], and one must include higher-order derivatives to ensure stability. In a few select cases, expressions of the form (5) and (10) can be systematically derived [38, 50, 71]. Generally, one can regard the free-energy expansion (10) as an effective field theory whose phenomenological parameters can be determined from experiments. This approach has proved successful for dense bacterial suspensions [34, 35] and now also for ALCs, indeed suggesting some universality in the formation and dynamics of topological defects in active systems.

**Nematic defect order.** Although  $(\gamma_2, D)$  are varied as independent effective parameters in the simulations, they are likely coupled through underlying physical and chemical parameters. For example, it is plausible that a change in ATP-concentration or film-thickness would affect both  $\gamma_2$  and  $D$ . The parameter  $D$  can also be interpreted as an effective Reynolds number. In our numerical exploration of the  $(\gamma_2, D)$ -parameter space, we observe for subcritical advection  $D$  either long-lived lattice-like states exhibiting nematically aligned  $+\frac{1}{2}$ -defects or defect-free ground-states (Fig. 2; Movies S3, S4, S5 and S6). Ordered defect configurations correspond to local minima or saddles in the free-energy landscape and have only slightly higher energy than defect-free states (Fig. 2c). When the activity  $\zeta$  is sufficiently large that advection is marginally supercritical,  $D \gtrsim D_c$ , chaotic system trajectories spend a considerable time in the vicinity of these metastable lattice states, which provides

a physical basis for the orientational order of defects in thin ALC films [46]. For  $D \gg D_c$ , the ALC system can access a wider range of high-energy states, leading to increased disorder in the defect dynamics. Although the strongly turbulent regime  $D \gg D_c$  requires high time-resolution and is thus difficult to realize in long-time simulations, the inhibition of nematic defect order at larger values of  $D$  is evident from the reduced peak heights in Fig. 5c and d.

**Defect statistics.** The systematic speed deficit in Fig. 6c likely reflects the overdamped closure condition (7), which suppresses the propagation of hydrodynamic excitations. Since flow in a newly created defect pair generally points from the  $-\frac{1}{2}$  to the  $+\frac{1}{2}$ -defect, the minimal model (11) can be expected to underestimate the speeds of  $+\frac{1}{2}$ -defects. This effect could be explored in future experiments through a controlled variation of the thickness and viscosity of the oil film (Fig. 1a). The low-probability tail of long-living  $+\frac{1}{2}$ -defects in the simulation data (Fig. 6d) may be due to the fact that they can be tracked indefinitely in the simulations but are likely to leave the finite field of view in the experiments. In the future, the minimal theory presented here should be extended systematically by adding physically permissible extra terms [72] to the free-energy, explicitly simulating the full hydrodynamics in Eq. (6), or incorporating additional terms into Eq. (4) that account for the interaction between the nematic field and the induced flow [62, 72]. Such extensions will likely improve further the quantitative agreement between experiment and theory.

## CONCLUSIONS

Recent experimental and theoretical studies showed that fourth-order PDE models for scalar and vector fields provide an accurate quantitative description of surface-pattern formation in soft elastic materials [38] and orientational order in dense bacterial fluids [34, 35]. Here, we have generalized these ideas to matrix-valued fields describing soft active nematics. The above analysis demonstrates that a generic fourth-order  $Q$ -tensor model can shed light on previously unexplained experimental observations in 2D ALCs [46], including the emergence of

orientational order of topological defects. The fact that three vastly different soft matter systems can be treated quantitatively in terms of structurally similar higher-order PDEs [34, 35, 38] promises a unified mathematical framework for the description of pattern formation processes in a broad class of complex materials. In addition, the free-energy analogy [51] between dense ALCs and generalized Gross-Pitaevskii models suggests that the self-organization principles [33] of mesoscopic active matter and microscopic quantum systems [54–57] could be more similar than previously thought.

**Acknowledgments.** This work was supported by the NSF Mathematical Sciences Postdoctoral Research Fellowship DMS-1400934 (A.O.), an MIT Solomon Buchsbaum Fund Award (J.D.) and an Alfred P. Sloan Research Fellowship (J.D.). The authors would like to thank Zvonimir Dogic and Stephen DeCamp for kindly sharing their experimental data and details of their experiments, and Michael Hagan, Jean-Francois Joanny, Ken Kamrin, Mehran Kardar, Cristina Marchetti, Jonasz Slomka, Norbert Stoop, Francis Woodhouse and Martin Zwierlein for insightful discussions and helpful comments.

## METHODS

**Numerical solver & defect tracking.** To simulate Eq. (11), we implemented a numerical algorithm that evolves the real and imaginary parts  $\lambda(t, \mathbf{r})$  and  $\mu(t, \mathbf{r})$  of the complex order parameter  $\psi$  in time for periodic boundary conditions in space. The algorithm solves Eq. (11) pseudospectrally in space using  $N_\ell = 256$  or  $N_\ell = 512$  lattice points in each direction. Spectral analysis shows that  $N_\ell = 256$  is generally sufficient to resolve the fine-structure of the numerical solutions (Supplementary Fig. S6). The algorithm steps forward in time using a modified exponential time-differencing fourth-order Runge-Kutta method [68] with time step  $\Delta t \leq 2^{-10}$ . Simulations were initialized with either a single defect pair or random field configurations  $\{\lambda(0, \mathbf{r}), \mu(0, \mathbf{r})\}$ . Defects are located at the intersections of the zero-contours of  $\lambda$  and  $\mu$ , their positions tracked by implementing James Munkres' variant of the Hungarian assignment algorithm [73] (Supplementary Information).

- 
- [1] M. A. McEvoy and N. Correll. Materials that couple sensing, actuation, computation, and communication. *Science*, 347(6228), 2015.
  - [2] S. M. Douglas, A. H. Marblestone, S. Teerapittayanon, A. Vazquez, G. M. Church, and W. M. Shih. Rapid prototyping of 3D DNA-origami shapes with caDNAno. *Nucl. Acids Res.*, 37(15):5001–5006, 2009.
  - [3] V. Schaller, C. Weber, C. Semmrich, E. Frey, and A. R. Bausch. Polar patterns of driven filaments. *Nature*, 467:73–77, 2010.
  - [4] Y. Sumino, K. H. Nagai, Y. Shitaka, D. Tanaka, K. Yoshikawa, H. Chaté, and K. Oiwa. Large-scale vortex lattice emerging from collectively moving microtubules. *Nature*, 483:448–452, 2012.
  - [5] T. Sanchez, D. T. N. Chen, S. J. DeCamp, M. Heymann, and Z. Dogic. Spontaneous motion in hierarchically assembled active matter. *Nature*, 491:431, 2012.
  - [6] P. W. K. Rothmund. Folding DNA to create nanoscale shapes and patterns. *Nature*, 440(7082):297–302, 03 2006.
  - [7] P. C. Nickels, Y. Ke, R. Jungmann, D. M. Smith, M. Leichsenring, W. M. Shih, T. Liedl, and B. Högberg. DNA

- Origami Structures Directly Assembled from Intact Bacteriophages. *Small*, 10(9):1765–1769, 2014.
- [8] A. R. Studart and R. M. Erb. Bioinspired materials that self-shape through programmed microstructures. *Soft Matter*, 10:1284–1294, 2014.
- [9] J. Toner and Y. Tu. Flocks, herds, and schools: A quantitative theory of flocking. *Phys. Rev. E*, 58(4):4828–4858, 1998.
- [10] R. A. Simha and S. Ramaswamy. Hydrodynamic fluctuations and instabilities in ordered suspensions of self-propelled particles. *Phys. Rev. Lett.*, 89(5):058101, 2002.
- [11] D. Saintillan and M. Shelley. Instabilities, pattern formation and mixing in active suspensions. *Phys. Fluids*, 20:123304, 2008.
- [12] L. Giomi, L. Mahadevan, B. Chakraborty, and M. F. Hagan. Excitable patterns in active nematics. *Phys. Rev. Lett.*, 106:218101, 2011.
- [13] F. Peruani, F. Ginelli, M. Bär, and H. Chaté. Polar vs. apolar alignment in systems of polar self-propelled particles. *J. Phys.: Conf. Ser.*, 297:012014, 2011.
- [14] A. Peshkov, I. S. Aranson, E. Bertin, H. Chaté, and F. Ginelli. Nonlinear field equations for aligning self-propelled rods. *Phys. Rev. Lett.*, 109:268701, 2012.
- [15] M. Ravnik and J. M. Yeomans. Confined active nematic flow in cylindrical capillaries. *Phys. Rev. Lett.*, 110:026001, 2013.
- [16] T. C. Adhyapak, S. Ramaswamy, and J. Toner. Live soap: Stability, order, and fluctuations in apolar active smectics. *Phys. Rev. Lett.*, 110:118102, 2013.
- [17] M. C. Marchetti, J. F. Joanny, S. Ramaswamy, T. B. Liverpool, J. Prost, M. Rao, and R. A. Simha. Hydrodynamics of soft active matter. *Rev. Mod. Phys.*, 85:1143, 2013.
- [18] T. Gao, R. Blackwell, M. A. Glaser, M. D. Betterton, and M. J. Shelley. Multiscale polar theory of microtubule and motor-protein assemblies. *Phys. Rev. Lett.*, 114:048101, 2015.
- [19] L. Giomi. Geometry and topology of turbulence in active nematics. *Phys. Rev. X*, 5:031003, 2015.
- [20] C. A. Mirkin, R. L. Letsinger, R. C. Mucic, and J. J. Storhoff. A DNA-based method for rationally assembling nanoparticles into macroscopic materials. *Nature*, 382(6592):607–609, 1996.
- [21] M.-P. Valignat, O. Theodoly, J. C. Crocker, W. B. Russel, and P. M. Chaikin. Reversible self-assembly and directed assembly of DNA-linked micrometer-sized colloids. *Proc. Natl. Acad. Sci. U.S.A.*, 102(12):4225–4229, 2005.
- [22] J. Palacci, S. Sacanna, A. P. Steinberg, D. J. Pine, and P. M. Chaikin. Living crystals of light-activated colloidal surfers. *Science*, 339(6122):936–940, 2013.
- [23] W. Ebeling, A. Engel, and R. Feistel. *Physik der Evolutionsprozesse*. Akademie Verlag, 1992.
- [24] Z. Zeravcic and M. P. Brenner. Self replicating colloidal clusters. *Proc. Natl. Acad. Sci. U.S.A.*, 111(5):1748–1753, 2014.
- [25] J. L. England. Statistical physics of self-replication. *J. Chem. Phys.*, 139:121923, 2013.
- [26] B. Berger, P. W. Shor, L. Tucker-Kellogg, and J. King. Local rule-based theory of virus shell assembly. *Proc. Natl. Acad. Sci. U.S.A.*, 91(16):7732–7736, 1994.
- [27] J. D. Perlmutter and M. F. Hagan. Mechanisms of virus assembly. *Annu. Rev. Phys. Chem*, 66:217–239, 2015.
- [28] G. Meng, J. Paulose, D. R. Nelson, and V. N. Manoharan. Elastic instability of a crystal growing on a curved surface. *Science*, 343(6171):634–637, 2014.
- [29] A. Baskaran and M. C. Marchetti. Hydrodynamics of self-propelled hard rods. *Phys. Rev. E*, 77:011920, 2008.
- [30] A. Baskaran and M. C. Marchetti. Statistical mechanics and hydrodynamics of bacterial suspensions. *Proc. Natl. Acad. Sci.*, 106(37):15567–15572, 2009.
- [31] T. Vicsek and A. Zafeiris. Collective motion. *Physics Reports*, 517(3-4):71–140, 2012.
- [32] S. Ramaswamy. The mechanics and statistics of active matter. *Annu. Rev. Cond. Mat. Phys.*, 1:323–345, 2010.
- [33] N. Goldenfeld and C. Woese. Life is physics: Evolution as a collective phenomenon far from equilibrium. *Annual Rev. Cond. Mat. Phys.*, 2(1):375–399, 2011.
- [34] H. H. Wensink, J. Dunkel, S. Heidenreich, K. Drescher, R. E. Goldstein, H. Löwen, and J. M. Yeomans. Mesoscale turbulence in living fluids. *Proc. Natl. Acad. Sci. USA*, 109(36):14308–14313, 2012.
- [35] J. Dunkel, S. Heidenreich, K. Drescher, H. H. Wensink, M. Bär, and R. E. Goldstein. Fluid dynamics of bacterial turbulence. *Phys. Rev. Lett.*, 110:228102, 2013.
- [36] C. A. Weber, T. Hanke, J. Deseigne, S. Léonard, O. Dauchot, E. Frey, and H. Chaté. Long-range ordering of vibrated polar disks. *Phys. Rev. Lett.*, 110:208001, 2013.
- [37] R. Suzuki, C. A. Weber, E. Frey, and A. Bausch. Polar pattern formation in driven filament systems require non-binary particle collisions. *Nature Physics*, 11:839–843, 2015.
- [38] N. Stoop, R. Lagrange, D. Terwagne, P. M. Reis, and J. Dunkel. Curvature-induced symmetry breaking determines elastic surface patterns. *Nature Materials*, 14:337–342, 2015.
- [39] A. Sokolov and I. S. Aranson. Physical properties of collective motion in suspensions of bacteria. *Phys. Rev. Lett.*, 109:248109, 2012.
- [40] M. Cross and H. Greenside. *Pattern Formation and Dynamics in Nonequilibrium Systems*. Cambridge University Press, Cambridge, England, 2009.
- [41] P. G. de Gennes and J. Prost. *The Physics of Liquid Crystals*, volume 2. Oxford University Press, Oxford, 1995.
- [42] V. Narayan, S. Ramaswamy, and N. Menon. Long-lived giant number fluctuations in a swarming granular nematic. *Science*, 317:105–108, 2007.
- [43] I. S. Aranson, A. Snezhko, J. S. Olafsen, and J. S. Urbach. Comment on "Long-Lived Giant Number Fluctuations in a Swarming Granular Nematic". *Science*, 320(5876):612, 2008.
- [44] X.-q. Shi and Y.-q. Ma. Topological structure dynamics revealing collective evolution in active nematics. *Nat. Commun.*, 4:3013, 2013.
- [45] F. C. Keber, E. Loiseau, T. Sanchez, S. J. DeCamp, L. Giomi, M. J. Bowick, M. C. Marchetti, Z. Dogic, and A. R. Bausch. Topology and dynamics of active nematic vesicles. *Science*, 345(6201):1135–1139, 2014.
- [46] S. J. DeCamp, G. S. Redner, A. Baskaran, M. F. Hagan, and Z. Dogic. Orientational order of motile defects in active nematics. *Nature Materials*, 14:1110–1115, 2015.
- [47] I. Musevic, M. Skarabot, U. Tkalec, M. Ravnik, and S. Zumer. Two-dimensional nematic colloidal crystals self-assembled by topological defects. *Science*, 313(5789):954–958, 2006.
- [48] T. Machon and G. P. Alexander. Knots and nonorientable surfaces in chiral nematics. *Proceedings of the National Academy of Sciences*, 110(35):14174–14179, 2013.

- [49] U. Tkalec, M. Ravnik, S. Copar, S. Zumer, and I. I. Musevic. Reconfigurable knots and links in chiral nematic colloids. *Science*, 333(6038):62–65, 2011.
- [50] J. Swift and P. C. Hohenberg. Hydrodynamic fluctuations at the convective instability. *Phys. Rev. A*, 15(1):319–328, 1977.
- [51] S. R. Renn and T. C. Lubensky. Abrikosov dislocation lattice in a model of the cholesteric-to-smectic-*A* transition. *Phys. Rev. A*, 38:2132–2147, Aug 1988.
- [52] E. P. Gross. Structure of a quantized vortex in boson systems. *Nuovo Cim.*, 20(3):454–477, 1961.
- [53] L. P. Pitaevskii. Vortex lines in an imperfect Bose gas. *Sov. Phys. JETP*, 13(2):451–454, 1961.
- [54] J. Higbie and D. M. Stamper-Kurn. Periodically dressed Bose-Einstein condensate: A superfluid with an anisotropic and variable critical velocity. *Phys. Rev. Lett.*, 88:090401, 2002.
- [55] Y. J. Lin, K. Jimenez-Garcia, and I. B. Spielman. Spin-orbit-coupled Bose-Einstein condensates. *Nature*, 471(7336):83–86, 2011.
- [56] L. W. Cheuk, A. T. Sommer, Z. Hadzibabic, T. Yefsah, W. S. Bakr, and M. W. Zwierlein. Spin-injection spectroscopy of a spin-orbit coupled Fermi gas. *Phys. Rev. Lett.*, 109:095302, 2012.
- [57] C. V. Parker, L.-C. Ha, and C. Chin. Direct observation of effective ferromagnetic domains of cold atoms in a shaken optical lattice. *Nat. Phys.*, 9(12):769–774, 2013.
- [58] P. G. de Gennes. An Analogy between Superconductors and Smectics A. *Solid State Comm.*, 10:753–756, 1972.
- [59] J. W. Goodby, M. A. Waugh, S. M. Stein, E. Chin, R. Pindak, and J. S. Patel. Characterization of a new helical smectic liquid crystal. *Nature*, 337:449–552, 1989.
- [60] G. Srajer, R. Pindak, M. A. Waugh, and J. W. Goodby. Structural measurements on the liquid-crystal analog of the Abrikosov phase. *Phys. Rev. Lett.*, 64(13):1545–1548, 1990.
- [61] S. P. Thampi, R. Golestanian, and J. M. Yeomans. Velocity correlations in an active nematic. *Phys. Rev. Lett.*, 111:118101, 2013.
- [62] L. Giomi, M. J. Bowick, X. Ma, and M. C. Marchetti. Defect annihilation and proliferation in active nematics. *Phys. Rev. Lett.*, 110:228101, 2013.
- [63] A. Sokolov, I. S. Aranson, J. O. Kessler, and R. E. Goldstein. Concentration dependence of the collective dynamics of swimming bacteria. *Phys. Rev. Lett.*, 98:158102, 2007.
- [64] R. H. Kraichnan and D. Montgomery. Two-dimensional turbulence. *Rep. Prog. Phys.*, 43:547–619, 1980.
- [65] H. Kellay and W. I. Goldburg. Two-dimensional turbulence: a review of some recent experiments. *Rep. Prog. Phys.*, 65:845–894, 2002.
- [66] F. G. Woodhouse and R. E. Goldstein. Cytoplasmic streaming in plant cells emerges naturally by microfilament self-organization. *Proc. Natl. Acad. Sci. U.S.A.*, 110(35):14132–14137, 2013.
- [67] R. Voituriez, J. F. Joanny, and J. Prost. Generic phase diagram of active polar films. *Phys. Rev. Lett.*, 96(028102), 2006.
- [68] A.-K. Kassam and L. N. Trefethen. Fourth-order time-stepping for stiff PDEs. *SIAM J. Sci. Comput.*, 26(4):1214–1233, 2005.
- [69] A. J. Vromans and L. Giomi. Orientational properties of nematic disclinations. 2015. arXiv:1507.05588.
- [70] I. S. Aranson and L. S. Tsimring. Patterns and collective behavior in granular media: Theoretical concepts. *Rev. Mod. Phys.*, 78:641–692, 2006.
- [71] R. Großmann, P. Romanczuk, M. Bär, and L. Schimansky-Geier. Vortex arrays and mesoscale turbulence of self-propelled particles. *Phys. Rev. Lett.*, 113:258104, 2014.
- [72] H. Stark and T. C. Lubensky. Poisson-bracket approach to the dynamics of nematic liquid crystals. *Phys. Rev. E*, 67:061709, 2003.
- [73] J. Munkres. Algorithms for assignment and transportation problems. *J. Soc. Indust. Appl. Math.*, 5(1):32–38, 1957.